Journal of
Micro/Nanolithography,
MEMS, and MOEMS

Nanolithography.SPIEDigitalLibrary.org

Measurement of EUV lithography pupil amplitude and phase variation via image-based methodology

Zachary Levinson
Erik Verduijn
Obert R. Wood
Pawitter Mangat
Kenneth A. Goldberg
Markus P. Benk
Antoine Wojdyla
Bruce W. Smith

SPIE.

Zachary Levinson, Erik Verduijn, Obert R. Wood, Pawitter Mangat, Kenneth A. Goldberg, Markus P. Benk, Antoine Wojdyla, Bruce W. Smith, "Measurement of EUV lithography pupil amplitude and phase variation via image-based methodology," *J. Micro/Nanolith. MEMS MOEMS* **15**(2), 023508 (2016), doi: 10.1117/1.JMM.15.2.023508.

Measurement of EUV lithography pupil amplitude and phase variation via image-based methodology

Zachary Levinson,[a,*] Erik Verduijn,[b] Obert R. Wood,[b] Pawitter Mangat,[b] Kenneth A. Goldberg,[c] Markus P. Benk,[c] Antoine Wojdyla,[c] and Bruce W. Smith[a]
[a]Rochester Institute of Technology, 168 Lomb Memorial Drive, Rochester, New York 14623, United States
[b]GLOBALFOUNDRIES, 400 Stone Break Road Extension, Malta, New York 12020, United States
[c]Lawrence Berkeley National Laboratory, One Cyclotron Road, Berkeley, California 94720, United States

Abstract. An approach to image-based EUV aberration metrology using binary mask targets and iterative model-based solutions to extract both the amplitude and phase components of the aberrated pupil function is presented. The approach is enabled through previously developed modeling, fitting, and extraction algorithms. We seek to examine the behavior of pupil amplitude variation in real-optical systems. Optimized target images were captured under several conditions to fit the resulting pupil responses. Both the amplitude and phase components of the pupil function were extracted from a zone-plate-based EUV mask microscope. The pupil amplitude variation was expanded in three different bases: Zernike polynomials, Legendre polynomials, and Hermite polynomials. It was found that the Zernike polynomials describe pupil amplitude variation most effectively of the three. [DOI: 10.1117/1.JMM.15.2.023508]

Keywords: EUV lithography; EUV aberrations; EUV transmission function; aberration metrology; image-based aberration metrology; pupil characterization.

Paper 16025P received Mar. 18, 2016; accepted for publication Jun. 7, 2016; published online Jun. 28, 2016.

1 Introduction

For several lithography generations, pupil plane characterization has played a critical role in image process optimization.[1–3] This continues into EUV lithography (EUVL) with an additional importance placed on the understanding of the influences and variations of aberration behavior during system operation.[4,5] Interferometric methods have been shown to have subnanometer accuracy and are the *de facto* standard of aberration metrology but require additional optics.[6–8] Therefore, such methods can be challenging to implement during tool use, especially where EUV wavelengths introduce additional constraints. To this end, we have developed a method to measure optical aberrations of an EUV optical system using images formed by that system.[9–12]

In past studies, traditional aberration theory has focused on studying the pupil phase variation of imaging systems. This type of variation affects the shape of a point source traveling through the system but does not adequately account for other types of variation.[10,11,13–15] These other types of system variation are usually assumed to be small enough to not affect longer wavelength imaging, but they are important in EUV imaging. For example, even slightly misaligned lens elements can cause a variation in amplitude across the pupil.[16] More specific to EUVL, the multilayer reflectivity can vary dramatically as a function of incidence angle. This introduces a diffraction intensity imbalance in partially coherent imagery.[17] This intensity imbalance can cause image variation through focus.[18,19] Any optical system can be affected by this type of variation, but these effects become non-negligible with the tighter tolerances of EUVL systems. For this reason, we have adopted a more general definition of system aberration: any variation during imaging which introduces error to the pupil.

We aim to show that an enhanced image-based method is flexible enough to account for such error through exploration of both phase and amplitude variation in an EUV imaging system. This approach is enabled via iterative inverse solutions based on nonlinear least squares fitting of vector aerial image simulations. We examine the flexibility and criticality of the method by extracting the pupil phase and amplitude variation of zone plate lenses on an EUV mask microscope, the Semiconductor High-NA Actinic Reticle Review Project (SHARP) at Lawrence Berkeley National Laboratory.[20,21] To study the key characteristics of amplitude variation, the pupil amplitude function is expanded in three different bases.

2 Principles of Pupil Variation

2.1 *Modeling Pupil Variation*

The transfer of light through an optical system can be given as

$$\widetilde{E}_i(u,v) = \widetilde{E_o}(u,v) \cdot P(u,v), \tag{1}$$

where $\widetilde{E}(u,v)$ represents the frequency domain representation of the electric field $E(x,y)$ and $P(u,v)$ is the pupil function.[22,23]

The pupil function is complex valued and can, therefore, be expressed in terms of its amplitude and phase as

$$P(u,v) = \alpha(u,v)e^{i2\pi W(u,v)}. \tag{2}$$

The pupil wavefront, $W(u,v)$, is defined in units of waves (or a percentage of the actinic wavelength). These two

*Address all correspondence to: Zachary Levinson, E-mail: zal2186@rit.edu

1932-5150/2016/$25.00

functions, $\alpha(u,v)$ and $W(u,v)$, describe the phase difference between the object electric field and a Gaussian reference wavefront. In an ideal system, $W(u,v)$ is zero across the pupil at best focus and increases quadratically across the pupil with defocus.[23,24] Traditionally, an imaging system is said to be aberrated when $W(u,v)$ is nonzero at best focus. It is often useful to express $W(u,v)$ in an orthogonal function expansion, which is most efficiently described by Zernike polynomials.[13,14,24]

This choice of a Zernike basis has three benefits: (1) a small number of terms are sufficient to describe the phase variation with minimal error, (2) each term has a direct physical interpretation, and (3) the Zernike polynomials provide a rotationally invariant basis. $W(u,v)$ expressed as a Zernike series is given by Eq. (3), where ρ and ϕ are defined in Eqs. (4) and (5)

$$W(u,v)=\sum_{N=0}^{\infty}a_N Z_N(\rho,\phi), \tag{3}$$

$$\rho=\sqrt{u^2+v^2}, \tag{4}$$

$$\phi=\arctan\left(\frac{v}{u}\right). \tag{5}$$

This description though accounts only for phase variation. It is customary to assume that any amplitude variation is small, uniform across the pupil, and negligible. To account for amplitude variations, we define the amplitude across the pupil as

$$\alpha(\rho,\phi)=\begin{cases}1+A(\rho,\phi) & :\rho\le 1,\\ 0 & :\rho>1,\end{cases} \tag{6}$$

where the function $A(\rho,\phi)$ represents any additional amplitude or reduction in amplitude across the pupil. From here, analysis of the amplitude variation is similar to that of the pupil phase function, which is the expansion of $A(\rho,\phi)$ in an orthogonal basis. The most efficient basis for the expansion then needs to be identified. One option is to expand the entire pupil function, $P(u,v)$, in Zernike polynomials.[25,26] This method requires a number of assumptions though, i.e., the pupil function must be azimuthally symmetric and the expansion coefficients become complex valued. Since we do not want to impose any *a priori* knowledge about the system and we want to maintain ease of physical interpretation, we will consider the pupil amplitude and phase variation separately.

2.2 *Properties of Various Orthogonal Bases*

In order to determine the required properties of the ideal basis for EUV system amplitude pupil variation, we will first look at the basic properties of the three bases.

2.2.1 *Zernike polynomials*

The Zernike polynomials form a complete set of orthogonal polar polynomials over the unit circle. The azimuthal and radial components are generated separately and are given in Eqs. (7) and (8), respectively. The complete Zernike polynomial is then given by the product of Eqs. (7) and (8), where n and m are integers with $-n<m<n$ and even $n-m$.[14] The Zernike radial polynomials are commonly normalized so that $R_n^m(r=1)=1$ and $R_n^m(r=0)=0$ for $m\neq 0$.

$$\Phi_m(\phi)=\begin{cases}\sin m\phi,\\ \cos m\phi,\end{cases} \tag{7}$$

$$R_n^m(r)=\sum_{k=0}^{(n-m)/2}(-1)^k\frac{(n-m)!}{k!\left(\frac{n+m}{2}-k\right)!\left(\frac{n-m}{2}-k\right)!}r^{n-2k}. \tag{8}$$

Any function defined over the unit circle, $f(r,\phi)$, can be expanded in terms of Zernike polynomials by solving the integral given by Eq. (9).[27] The Zernike polynomials are designed to be rotationally invariant, which means that the expansion coefficients of a version of f rotated by θ, given by $f(r,\phi-\theta)$, are only modified by a linear azimuthal phase term.[14] The Zernike moments of a rotated function are therefore given by Eq. (10). This can be seen by rotating the example image of Fig. 1(a) and then expanding it in Zernike polynomials. The choice of this image is arbitrary—any function defined over the unit circle is an equally valid choice. Some of the resulting Zernike moments are shown in Fig. 1(b), in which it is shown that the moments vary only by an azimuthal phase factor[27]

$$a_{|n|m}=\frac{n+1}{\pi}\int_{\phi=0}^{2\pi}\int_{r=0}^{1}f(r,\phi)R_n^m(r)e^{-im\phi}r\,\mathrm{d}r\,\mathrm{d}\phi, \tag{9}$$

$$a_{|n|m}^{(\theta)}=a_{|n|m}\cdot e^{-im\theta}. \tag{10}$$

Rotational invariance is useful in optical systems because a lens' aberrations should be independent of its rotation. For example, the total amount of third-order astigmatism in a lens will remain constant through the lens' rotation, though the amount of third-order astigmatism 90 deg (Z_5) and third-order astigmatism 45 deg (Z_6) contributing to this total third-order astigmatism may change. In other words, the quantity $a_5^2+a_6^2$ remains constant as a function of rotation angle, while a_5 and a_6 themselves change through rotation. This gives rise to the sinusoidal behavior of the moments in Fig. 1(b).

2.2.2 *Legendre polynomials*

The Legendre polynomials form a complete orthogonal set over the interval $-1\le x\le 1$. The polynomials can be generated via the Rodrigues' formula as follows:[28]

$$P_n(x)=\frac{1}{2^n n!}\frac{d^n}{dx^n}(x^2-1)^n, \tag{11}$$

where n is a positive integer. These polynomials are normalized so that the values at the edge of the interval are $P_n(x=1)=1$ and $P_n(x=-1)=(-1)^n$. Here, we extend the Legendre polynomials over the two-dimensional (2-D) Cartesian plane by using all the possible products of the Legendre polynomials in x and y. The first 36 of these products are given in Table 1. The notation $P_N^{(2)}$ is used to refer to the N'th product of two Legendre polynomials. This combination of polynomials is orthogonal over a unit square and fulfills the orthogonality condition

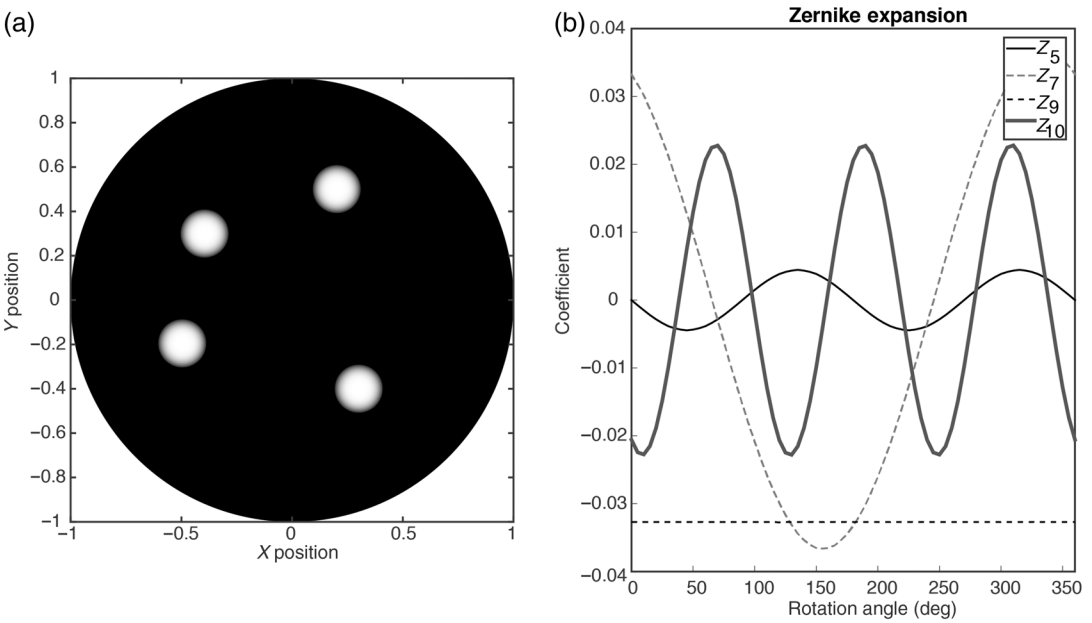

Fig. 1 (a) The image that was rotated and expanded in orthonormal bases. The units are normalized distance so that the function is defined over the unit circle. (b) Zernike expansion coefficients for third-order astigmatism, coma, spherical aberration, and trefoil for the image in part (a) through rotation.

Table 1 The first 36 Legendre polynomial combinations and Hermite polynomial combinations.

N	n_x	n_y	Legendre polynomial ($P_N^{(2)}$)	Hermite polynomial ($H_N^{(2)}$)
1	0	0	1	1
2	0	1	y	$2y$
3	1	0	x	$2x$
4	1	1	xy	$4xy$
5	0	2	$\frac{1}{2}(3y^2-1)$	$(4y^2-2)$
6	1	2	$\frac{x}{2}(3y^2-1)$	$2x(4y^2-2)$
7	2	0	$\frac{1}{2}(3x^2-1)$	$(4x^2-2)$
8	2	1	$\frac{y}{2}(3x^2-1)$	$(4x^2-2)2y$
9	2	2	$\frac{1}{4}(3x^2-1)(3y^2-1)$	$(4x^2-2)(4y^2-2)$
10	0	3	$\frac{1}{2}(5y^3-3y)$	$(8y^3-12y)$
11	1	3	$\frac{x}{2}(5y^3-3y)$	$2x(8y^3-12y)$
12	2	3	$\frac{1}{4}(3x^2-1)(5y^3-3y)$	$(4x^2-2)(8y^3-12y)$
13	3	0	$\frac{1}{2}(5x^3-3x)$	$(8x^3-12x)$
14	3	1	$\frac{y}{2}(5x^3-3x)$	$(8x^3-12x)2y$
15	3	2	$\frac{1}{4}(5x^3-3x)(3y^2-1)$	$(8x^3-12x)(4y^2-2)$
16	3	3	$\frac{1}{4}(5x^3-3x)(5y^3-3y)$	$(8x^3-12x)(8y^3-12y)$

Table 1 (*Continued*).

N	n_x	n_y	Legendre polynomial ($P_N^{(2)}$)	Hermite polynomial ($H_N^{(2)}$)
17	0	4	$\frac{1}{8}(35y^4 - 30y^2 + 3)$	$(16y^4 - 48y^2 + 12)$
18	1	4	$\frac{x}{8}(35y^4 - 30y^2 + 3)$	$2x(16y^4 - 48y^2 + 12)$
19	2	4	$\frac{1}{16}(3x^2 - 1)(35y^4 - 30y^2 + 3)$	$(4x^2 - 2)(16y^4 - 48y^2 + 12)$
20	3	4	$\frac{1}{16}(5x^3 - 3x)(35y^4 - 30y^2 + 3)$	$(8x^3 - 12x)(16y^4 - 48y^2 + 12)$
21	4	0	$\frac{1}{8}(35x^4 - 30x^2 + 3)$	$(16x^4 - 48x^2 + 12)$
22	4	1	$\frac{y}{8}(35x^4 - 30x^2 + 3)$	$(16x^4 - 48x^2 + 12)2y$
23	4	2	$\frac{1}{16}(35x^4 - 30x^2 + 3)(3y^2 - 1)$	$(16x^4 - 48x^2 + 12)(4y^2 - 2)$
24	4	3	$\frac{1}{16}(35x^4 - 30x^2 + 3)(5y^3 - 3y)$	$(16x^4 - 48x^2 + 12)(8y^3 - 12y)$
25	4	4	$\frac{1}{64}(35x^4 - 30x^2 + 3)(35y^4 - 30y^2 + 3)$	$(16x^4 - 48x^2 + 12)(16y^4 - 48y^2 + 12)$
26	0	5	$\frac{1}{8}(63y^5 - 70y^3 + 15y)$	$(32y^5 - 160y^3 + 120y)$
27	1	5	$\frac{x}{8}(63y^5 - 70y^3 + 15y)$	$2x(32y^5 - 160y^3 + 120y)$
28	2	5	$\frac{1}{16}(3x^2 - 1)(35y^4 - (63y^5 - 70y^3 + 15y)$	$(4x^2 - 2)(32y^5 - 160y^3 + 120y)$
29	3	5	$\frac{1}{16}(5x^3 - 3x)(63y^5 - 70y^3 + 15y)$	$(8x^3 - 12x)(32y^5 - 160y^3 + 120y)$
30	4	5	$\frac{1}{64}(35x^4 - 30x^2 + 3)(63y^5 - 70y^3 + 15y)$	$(16x^4 - 48x^2 + 12)(32y^5 - 160y^3 + 120y)$
31	5	0	$\frac{1}{8}(63x^5 - 70x^3 + 15x)$	$(32x^5 - 160x^3 + 120x)$
32	5	1	$\frac{y}{8}(63x^5 - 70x^3 + 15x)$	$(32x^5 - 160x^3 + 120x)2y$
33	5	2	$\frac{1}{16}(63x^5 - 70x^3 + 15x)(3y^2 - 1)$	$(32x^5 - 160x^3 + 120x)(4y^2 - 2)$
34	5	3	$\frac{1}{16}(63x^5 - 70x^3 + 15x)(5y^3 - 3y)$	$(32x^5 - 160x^3 + 120x)(8y^3 - 12y)$
35	5	4	$\frac{1}{64}(63x^5 - 70x^3 + 15x)(35y^4 - 30y^2 + 3)$	$(32x^5 - 160x^3 + 120x)(16y^4 - 48y^2 + 12)$
36	5	5	$\frac{1}{64}(63x^5 - 70x^3 + 15x)(63y^5 - 70y^3 + 15y)$	$(32x^5 - 160x^3 + 120x)(32y^5 - 160y^3 + 120y)$

$$C_{MN}\int_{x=-1}^{1}\int_{y=-1}^{1} P_M^{(2)}(x,y)P_N^{(2)}(x,y)\mathrm{d}x\,\mathrm{d}y = \delta_{MN}, \tag{12}$$

where δ_{MN} is the Kronecker delta and C_{MN} is an orthogonality constant.[29] This orthogonality condition would still be met if the set of polynomials was converted to polar coordinates. In the process of converting to polar coordinates, the limits of integration in Eq. (12) must be adjusted to the unit circle. We can, therefore, use this basis to express pupil variation because this set of polynomials is orthogonal over the unit circle.

Figure 2(a) shows the rotation of Fig. 1(a) and its subsequent expansion in Legendre polynomials. This time the variation in expansion coefficients is not a simple sinusoid, and therefore, the Legendre polynomials are not a rotationally invariant basis.

2.2.3 *Hermite polynomials*

The Hermite polynomials form a complete orthogonal set over the interval $-\infty \le x \le \infty$. The Rodrigues' formula for Hermite polynomials is given by Eq. (13).[28] There is no analytic formula for the value $H_n(x = \pm 1)$

$$H_n(x) = (-1)^n e^{x^2}\frac{d^n}{dx^n}e^{-x^2}. \tag{13}$$

Again, we extend the basis over the 2-D Cartesian plane by using all of the possible products of the Hermite polynomials in x and y. The first 36 of these products are shown in Table 1. The notation $H_N^{(2)}$ is used to refer to the N'th product of two Hermite polynomials. The same orthogonality argument made for Legendre polynomials holds for Hermite polynomials. Similarly, like Legendre polynomials, the Hermite polynomials are not rotationally invariant. This can be seen

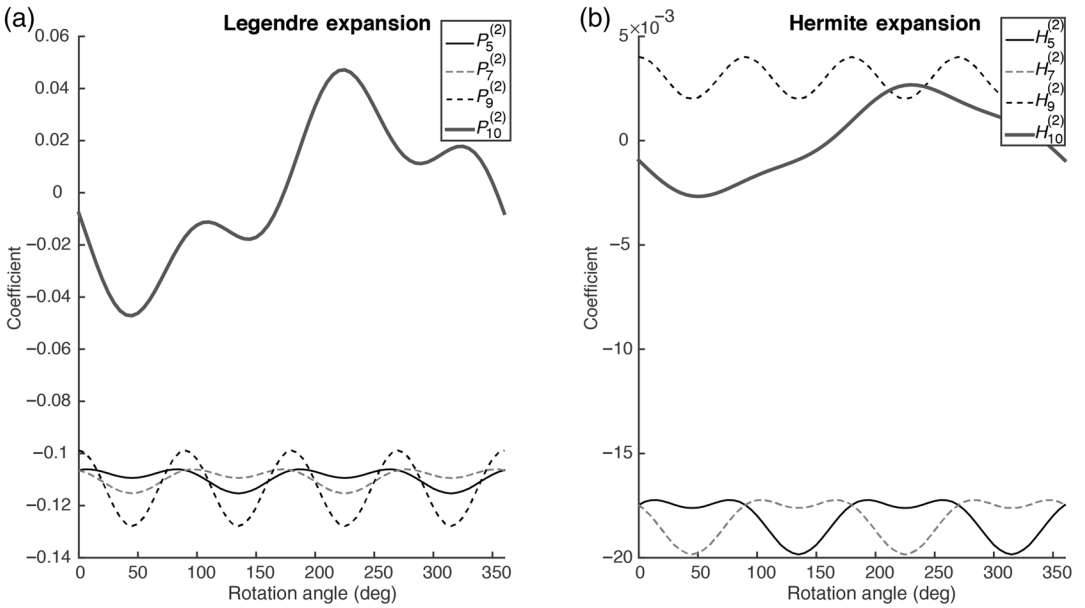

Fig. 2 The image in Fig. 1(a) was again rotated and expanded in Legendre polynomials and Hermite polynomials. The moments for (a) Legendre polynomials for $P_5^{(2)}$, $P_7^{(2)}$, $P_9^{(2)}$, $P_{10}^{(2)}$ and (b) Hermite polynomials for $H_5^{(2)}$, $H_7^{(2)}$, $H_9^{(2)}$, $H_{10}^{(2)}$ are plotted as a function of rotation angle.

again in Fig. 2(b), where Fig. 1(a) was rotated again and expanded this time in Hermite polynomials.

2.3 *Extraction of Pupil Phase Variation*

To measure optical aberrations of an EUVL system, experimental measurements of aberration sensitive patterns are iteratively fit to vector-based image simulations (PROLITH[30]) to determine the wavefront variation, as shown in Fig. 3. Specifically, we have identified a number of patterns that are most sensitive to a single aberration type, as shown in Fig. 4. These targets are optimized for each imaging system by balancing the aberration sensitivity and printability of the target. This target selection procedure is outlined in detail in Ref. 12. The lines orthogonal to the pattern in Fig. 4 represent the measurement locations. These types of patterns are present on many masks, so a special mask is often not necessary. These have been selected primarily so that there is a phase difference between measurement sites if a particular aberration is present. For example, the response used to estimate astigmatism is the difference in intensity between vertical and horizontal lines. Using the difference between structures provides an extremely robust aberration response.

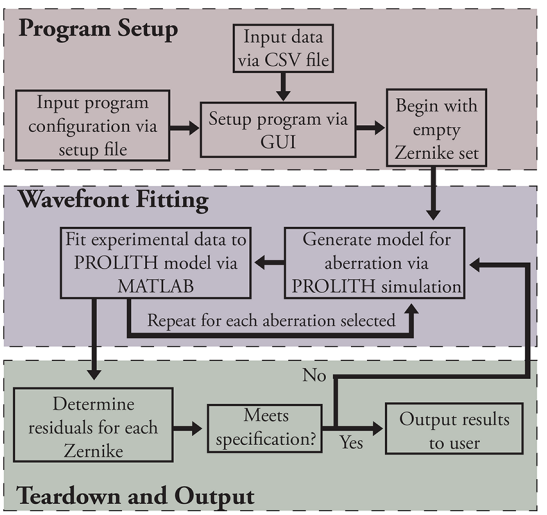

Fig. 3 Flowchart of the procedure used to extract pupil phase variation from image data.

The image data used to extract the phase variation can be either in the form of an aerial image or in the form of critical dimension (CD) measurements. After image data have been collected, they are iteratively fit to aerial image simulations. First an ideal wavefront is assumed; then an analytic model is constructed for each target response. For example, a model is fit to the vertical–horizontal CD difference through focus and astigmatism. Finally, the experimental data are fit to the analytical model to estimate the level of aberration. This process is repeated for each target to obtain an initial guess for the wavefront; then the process is repeated from the beginning. This fitting procedure is explored in further detail in Refs. 9–12.

2.4 *Extraction of Pupil Amplitude Variation*

Extraction of amplitude variation follows a similar procedure to that of phase variation, but is considered separately with a yet unknown basis. In the case of a fully coherent source, the diffracted energy from an ideal line-space grating can be approximated by a series of Bragg terms.[23,24] The locations within the pupil of these orders can be predicted by the grating equation, Eq. (14). The transfer of this diffracted energy through an imaging system can then be modeled by sampling the pupil function as in Eq. (1)

$$\rho = \frac{\lambda}{P \cdot NA}. \tag{14}$$

In the partially coherent case, analytic solutions prove considerably more difficult to obtain. The partial coherence

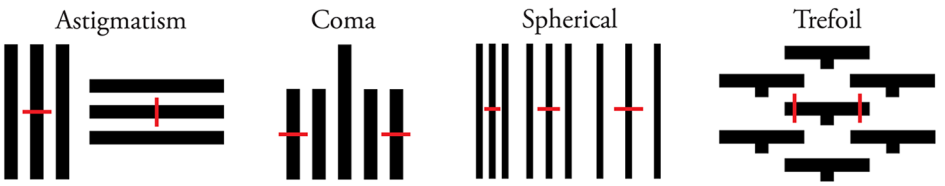

Fig. 4 Examples of the binary metrology targets used for inverse wavefront interrogation. The lines normal to the pattern denote the measurement locations. Each type of aberration is interrogated by a difference between two structures.

of the source can be considered to average the pupil function in those locations.[24,31,32] To reconstruct the pupil amplitude function $A(u, v)$, image data are iteratively fit to simulations to determine the values of the average value of the function over each diffraction order. This value corresponds to the source-averaged sample of the pupil amplitude function. This approach is identical to that used to extract pupil phase with one complication: the best choice of basis is unknown, so the source-averaged value of the amplitude function needs to be determined for each diffraction order instead of an expansion coefficient.

This pupil sampling process is shown in Fig. 5. The amplitude function can be reconstructed through interpolation after iteratively fitting samples. Barnes objective analysis is used to interpolate across the pupil between the samples.[33,34] This procedure—commonly used in meteorological modeling—uses an initial guess for each grid point, then iteratively refines it based on the error computed from the known values. The weight of each error is proportional to the inverse of its distance from other points.

To begin the objective analysis, we assume that the amplitude function $A(\rho, \phi)$ is Fourier decomposable. Then, a corresponding filtered function $\widetilde{A}(\rho, \phi)$ is constructed as

$$\widetilde{A}(\rho, \phi) = \int_{\theta=0}^{2\pi} \int_{r=0}^{\infty} A(\rho + r, \phi + \theta) W(r) r \mathrm{d}r \, \mathrm{d}\theta, \tag{15}$$

where r and θ are polar coordinates defined with respect to a point in the pupil (ρ, ϕ), and the filter $W(r)$ is given as

$$W(r) = \frac{1}{4\pi k} e^{-r^2/4k}, \tag{16}$$

where k is an arbitrary shape parameter. Equation (15) can be written in terms of the known discrete values of A as

$$\widetilde{A}_0(\rho, \phi) = \frac{\sum_{i=0}^{N} A_i e^{-r_i^2/4k}}{\sum_{i=0}^{N} e^{-r_i^2/4k}}, \tag{17}$$

where N is the number of known data points. A corrected amplitude function can then be computed from the smoothed error field as

$$\widetilde{A}_1(\rho, \phi) = \widetilde{A}_0 + \frac{\sum_{i=0}^{N} (A_i - \widetilde{A}_{0,i}) e^{-r_i^2/4\gamma k}}{\sum_{i=0}^{N} e^{-r_i^2/4\gamma k}}, \tag{18}$$

where γ is a number chosen to be between zero and one. This corrected field can be iteratively computed until the error reaches some prescribed limit. The effects of the choice of k and γ are discussed in detail in Refs. 33 and 34. This type of interpolation has the benefit of having high accuracy even when the samples are disordered and unevenly spaced. At this step, the amplitude function has been determined, but further expansion of the interpolated function in an orthogonal basis is useful. Zernike polynomials have been chosen in Fig. 5 because of the *a priori* knowledge that the original function was composed in this basis.

This method is able to reproduce the original function with little error from a small number of samples. To illustrate this, 500 random amplitude functions composed of third-order Zernike amplitude polynomials ($Z_A5 - Z_A11$) were sampled in $\rho = 0.5$ and $\rho = 0.9$ pupil zones with a partially coherent 0.1σ source. The amplitude functions were randomly generated with a mean range of 19.09% of the pupil transmission deviation. These functions were then reconstructed using the scheme proposed in Fig. 5. The root mean square (RMS) of each initial function varied, so it would be inappropriate to directly compare the RMS error (RMSE) from these cases. Instead, the error was normalized to the range of the original function to facilitate comparison. The normalized RMSE (NRMSE) (as a percentage of the range) closely follows a normal distribution with a

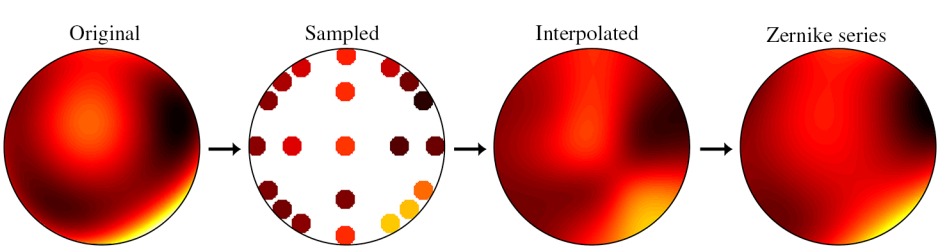

Fig. 5 Flowchart of pupil amplitude reconstruction. First, the pupil function is sampled via the diffracted spectrum of the targets used for phase interrogation. The values of these samples are determined via iterative fitting to aerial image simulations. Next, the Barnes analysis is used to interpolate between the samples to construct the original function. Finally, the interpolated function is expanded in a Fourier–Zernike series.

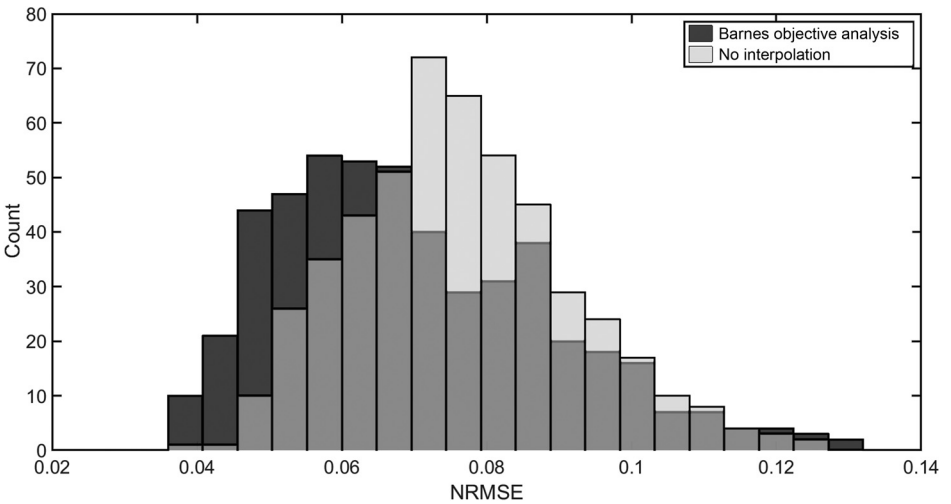

Fig. 6 NRMSE distribution of the reconstructed amplitude functions with and without interpolation via Barnes objective analysis. The distribution for functions reconstructed without interpolation is semitransparent to show the entirety of both distributions.

mean of 7.08% and a standard deviation of 1.96%. The NRMSE distribution of the 500 randomly generated functions is shown in Fig. 6, with and without the use of interpolation via Barnes objective analysis. It is clear that the use of interpolation decreases the mean NRMSE.

Closer inspection of Fig. 5 reveals that the error manifests itself as a smoothing of the original function. This can be seen by comparing the extracted series coefficients for one of the reconstructed functions to the exact coefficient, Fig. 7(a). The original functions were composed of random arrangements of third-order Zernike polynomials, but higher-order terms appear in the reconstructed function. This blurring effect is from the pupil-averaging of the partially coherent source, which can be reduced by increasing both the source coherence and the number of pupil samples. Still, the function can be reconstructed with little error with only the third-order Zernike polynomials used to compose the original function. This is compared to an expansion in the first 36 combinations of Cartesian Legendre polynomials [Fig. 7(b)], where the expansion would require more terms to reach a similar RMSE. This is verified by plotting the RMSE after adding each term for both series expansions, as in Fig. 7(c). In this plot, the RMSE decreases at a faster rate when the functions are expressed in a Zernike basis.

3 Simulation Study

In order to test the extraction error, 20 synthetic datasets were created for random wavefronts with both amplitude and phase aberrations. The average amplitude RMS was 29.9%, and the average phase RMS was 24.9 $m\lambda$. The proposed aberration extraction scheme lumps any high-order aberration terms into a single approximate low-order term. To investigate the error associated with lumping the high-order terms into the low-order terms, half of the synthetic datasets were composed of both third- and fifth-order Zernike polynomials. The other half is composed of only third-order Zernike polynomails, but the average wavefront RMS for each set is identical.

The average RMSE for each wavefront type is shown in Table 2. The amplitude RMSE was computed from a third-order Fourier–Zernike series of the interpolated amplitude function. As expected, the error increases when higher-order

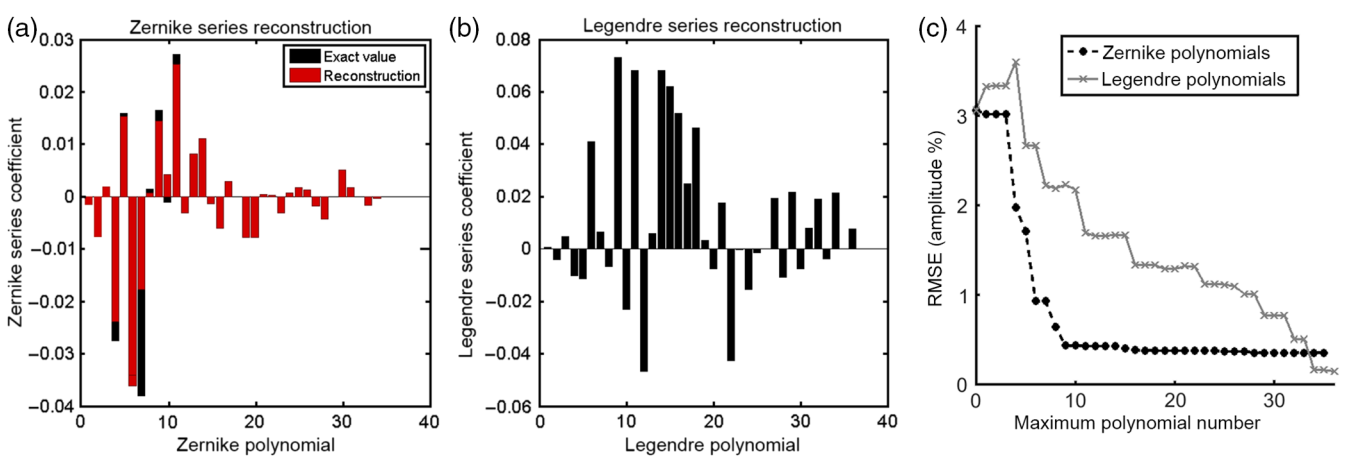

Fig. 7 Comparison of an orthogonal function expansion of an interpolated amplitude function in (a) Zernike polynomials and (b) the first 36 combinations of Cartesian Legendre polynomials. (c) The RMSE after adding each additional polynomial for both series expansions.

Table 2 Average RMSE for synthetic datasets composed of third-order Zernike polynomials (Z_5–Z_{11}) and both third- and fifth-order Zernike polynomials ($Z_5 - Z_{20}$).

Maximum aberration order	Amplitude RMSE (%)	Phase RMSE ($m\lambda$)
Third order	0.75	0.40
Fifth order	1.45	0.50

aberrations are lumped into lower-order terms. However, the error associated with aberration lumping is not substantial and remains at tolerable levels. The phase RMSE in Table 2 is comparable to that of past studies of the image-based method.[12]

4 Experimental Approach

The SHARP Actinic Reticle Review Project (SHARP) is a full-field EUV mask microscope at Lawrence Berkeley National Laboratory (LBNL). A schematic view of the system is shown in Fig. 8. SHARP forms a magnified image of an EUV mask onto a CCD sensor at 13.5-nm wavelength via interchangeable Fresnel zone plate lenses. The target CDs of the structures used for this experiment are given in Table 3. These values were determined by calculating the pitch required to sample the desired pupil location. Structures were chosen to sample $\rho = 0.5$ and $\rho = 0.9$ pupil zones.

All data were collected using a single 0.25 4 × NA lens on two separate days. In between these experiments, the system was modified, then realigned and recalibrated to the original condition. A 0.1σ circular illuminator was chosen to resemble a coherent source, while introducing a small amount of pupil averaging to decrease ringing effects. Each target was imaged through the full depth of focus at the smallest step available ± 2.7 μm in steps of 0.3 μm.

Images were analyzed with custom image processing software written in MATLAB®. SHARP has field-dependent aberrations, so image sequences were analyzed in similar field locations where SHARP is designed to be diffraction limited. After data collection, dark current noise from the CCD was subtracted from the images, then slight rotation and alignment errors were corrected. The image was then interpolated to a higher pixel grid, which also deconvolves the response of the CCD sensor. The images were collected at ~15 nm/px and interpolated to 5 nm/px. Finally, the interpolated region was averaged columnwise and normalized to obtain an approximate aerial image. A white point and a black point for normalization were chosen such that

Table 3 CDs of the metrology targets used for pupil function extraction on SHARP.

Aberration name	Structure type	Target CD (nm)
Astigmatism 90 deg	Vertical/horizontal line/space	30
Astigmatism 45 deg	45 deg /135 deg Line/space	30
Coma *X*	Vertical 5-bar	50
Coma *Y*	Horizontal 5-bar	50
Spherical	Line through pitch	30
Trefoil *X*	Horizontal T-Bar	35
Trefoil *Y*	Vertical T-Bar	35

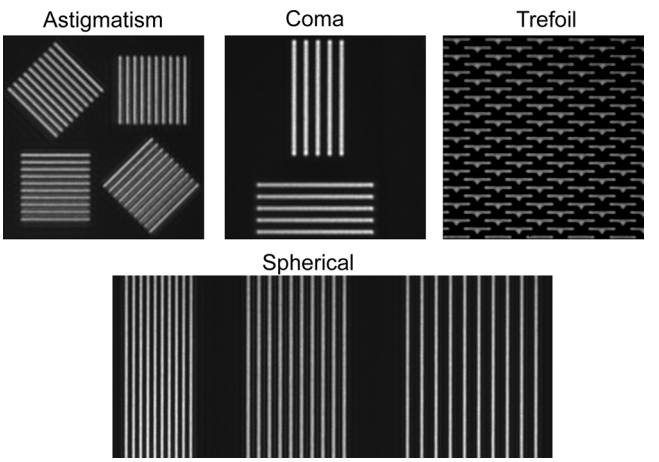

Fig. 9 Examples of the SHARP micrographs used for aerial image measurements to extract the aberrated amplitude and phase functions.

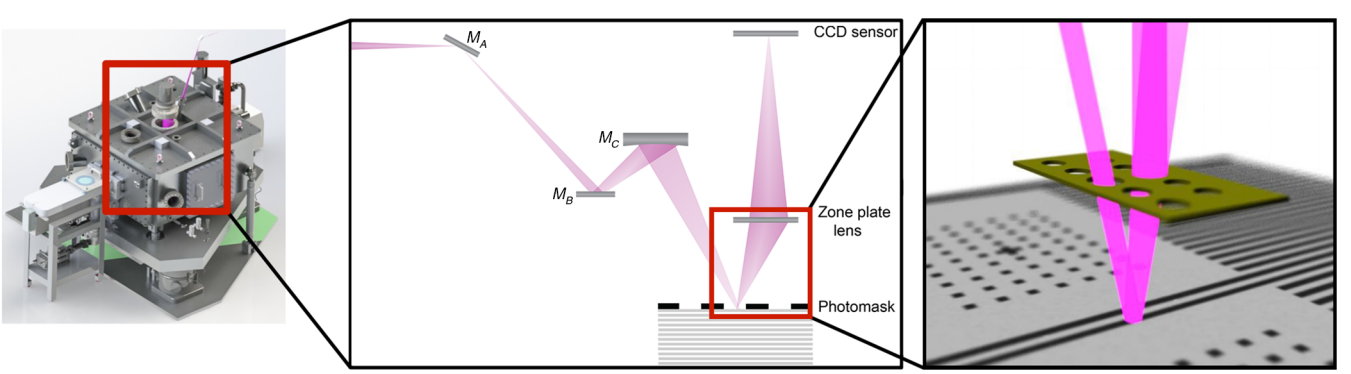

Fig. 8 A schematic view of the SHARP microscope at the advanced light source. EUV light at 13.5 nm from a bending magnet is focused on the photomask. The photomask is imaged on a CCD sensor using Fresnel zone plate lens.

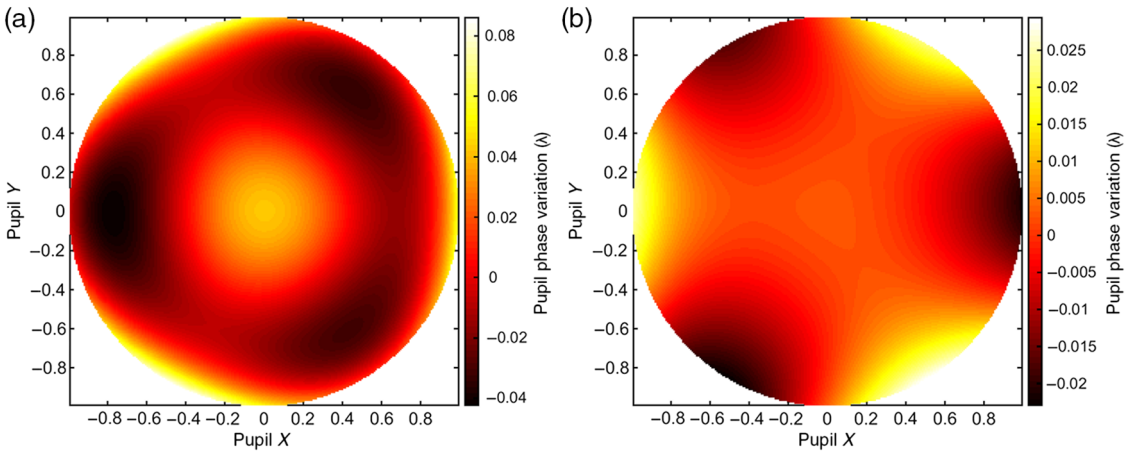

Fig. 10 Pupil phase variation on (a) day 1 and (b) day 2 extracted from the same 0.25 4xNA lens on LBNL SHARP EUV microscope via the proposed image-based method.

Table 4 Extracted Zernike coefficients and aerial image residual for SHARP after 10 iterations.

Aberration name	Day 1 extracted value ($m\lambda$)	Day 2 extracted value ($m\lambda$)
Astigmatism 90 deg	−11.66	−0.98
Astigmatism 45 deg	−2.61	−3.50
Coma X	0.00	0.00
Coma Y	0.00	0.00
Spherical	+42.71	+2.74
Trefoil X	+35.56	−23.19
Trefoil Y	0.00	0.00

the intensity-focus volume peaked at the ideal value at best focus, 1.29 for three-beam imaging.

Images were collected through focus, and the through focus intensity volume was used to extract the phase and amplitude functions. Third-order Zernike coefficients and amplitude function samples were determined from the intensity volume via an image-based method.[10,11,35] The amplitude function was then interpolated by Barnes objective analysis and expanded in Zernike polynomials, Hermite polynomials, and Legendre polynomials.

5 Imaging Results and Analysis

Examples of the images formed by SHARP for these experiments are given in Fig. 9. A total of 10 iterations (totaling 3.2 h of run-time on a machine with a 3.6-GHz quad-core Intel i7 processor and 16 GB of RAM) were needed for the wavefront extraction models to converge on a solution. The pupil phase variation extracted from the zone plate on day 1 is given in Fig. 10(a) and on day 2 in Fig. 10(b). The extracted third-order Zernike coefficients for each day are provided in Table 4. The wavefront has a phase RMS of

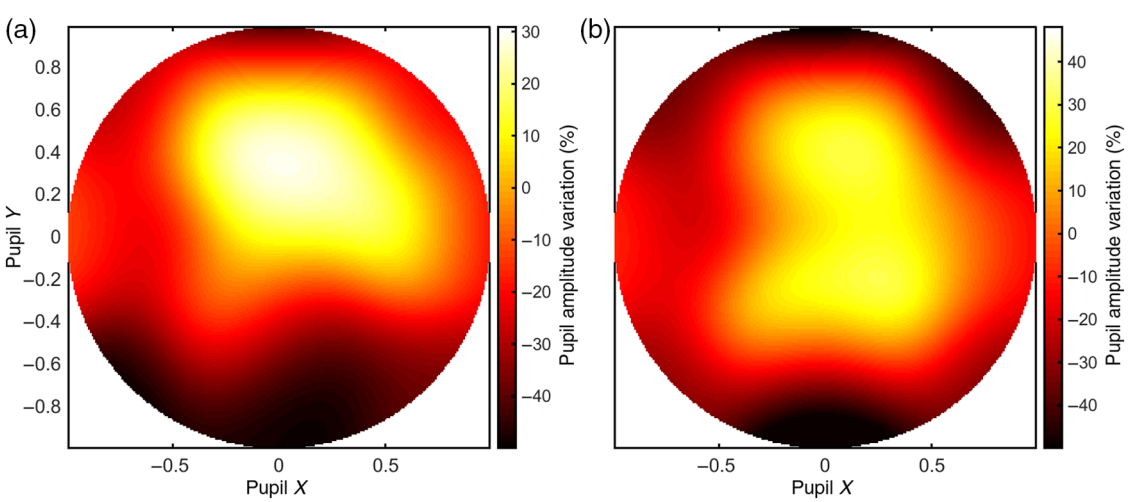

Fig. 11 Interpolated pupil amplitude variation on (a) day 1 and (b) day 2 from the LBNL SHARP EUV microscope via the proposed image-based method.

23.4 $m\lambda$ (0.316 nm) on day 1 and 8.4 $m\lambda$ (0.113 nm) on day 2.

The extracted pupil amplitude variation for day 1 is shown in Fig. 11(a) and for day 2 in Fig. 11(b). There was an amplitude RMS of 11% of the pupil transmission deviation on day 1 and an amplitude RMS of 12% of the pupil transmission deviation on day 2.

The SHARP pupil amplitude functions were expanded using Zernike amplitude polynomials, Hermite amplitude polynomials, and Legendre amplitude polynomials, as detailed earlier. The expansion coefficients for all three bases are plotted in Fig. 12 for day 1 and in Fig. 13 for day 2. As seen in both figures, the Legendre polynomial coefficients still vary significantly after 36 terms. This is an indication that Legendre polynomials are an inadequate choice of basis for pupil amplitude variation. In comparison, Figs. 12 and 13 suggest that Hermite polynomials may provide for a better choice of basis for pupil amplitude variation. The RMSE (with respect to the interpolated amplitude function) rate of change in Fig. 14 shows this not to be true, however. As seen, the RMSE decreases with each additional term at a rate of 2.9% per term, 1.6% per term, and 1.3% per term for Zernike polynomials, Hermite polynomials, and Legendre polynomials, respectively, on day 1 (defined as

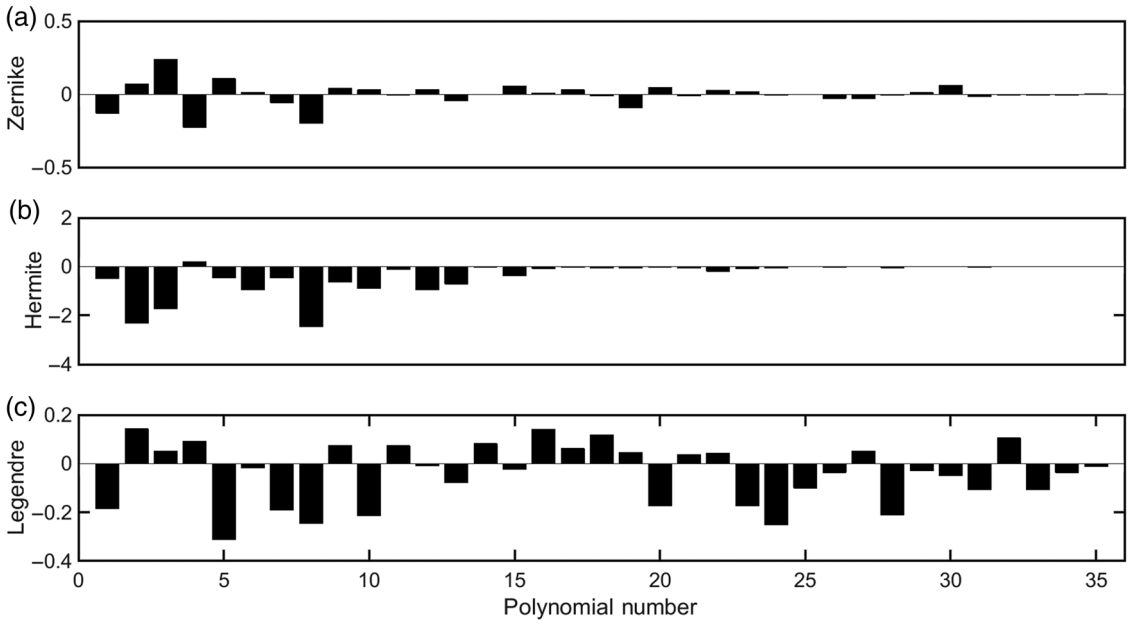

Fig. 12 Expansion coefficients for the pupil amplitude variation for day 1 expressed in (a) Zernike polynomials, (b) Hermite polynomials, and (c) Legendre polynomials.

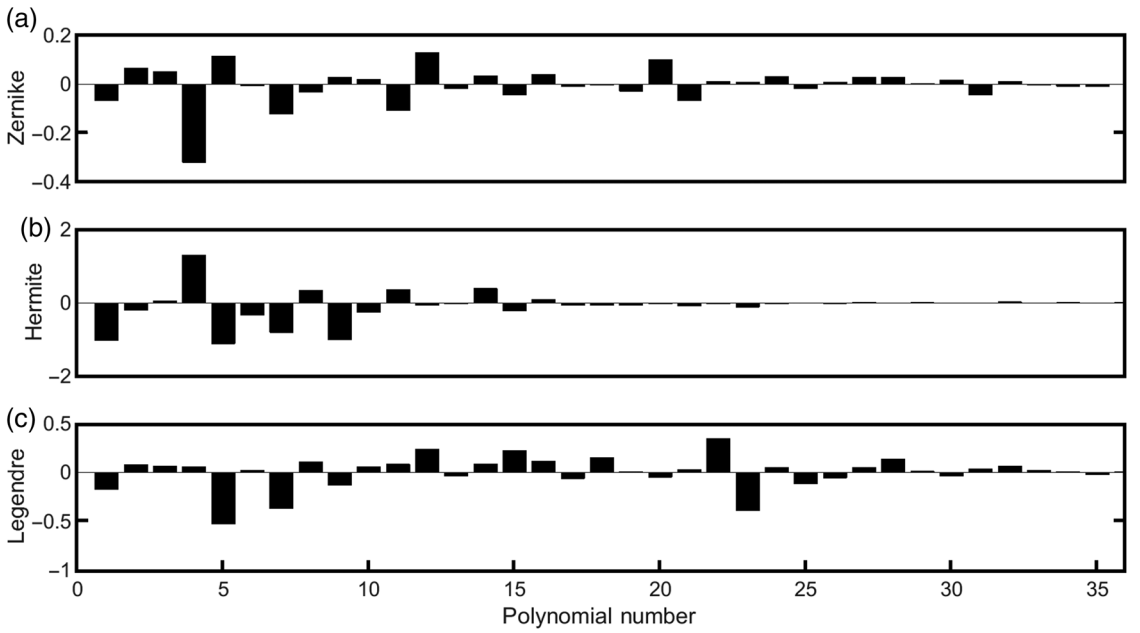

Fig. 13 Expansion coefficients for the pupil amplitude variation for day 2 expressed in (a) Zernike polynomials, (b) Hermite polynomials, and (c) Legendre polynomials.

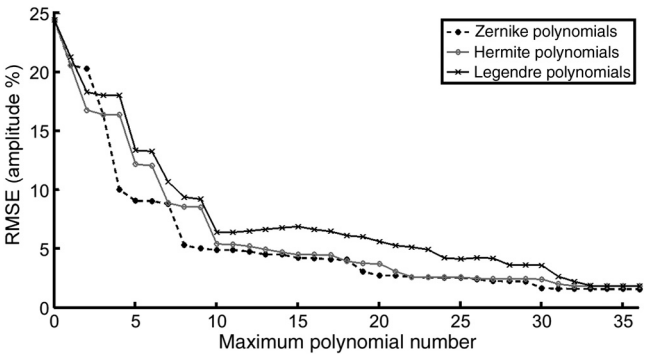

Fig. 14 The RMSE after adding each additional polynomial for Zernike polynomials, Legendre polynomial, and Hermite polynomial series expansions of the pupil amplitude variation extracted from day 1.

the slope of the secant line from zero to the fifth term of the series). Similarly, the RMSE rate of decrease is 2.4% per term, 0.3% per term, and 0.2% per term for Zernike polynomials, Hermite polynomials, and Legendre polynomials, respectively, on day 2. The RMSE rate of decrease is higher for Zernike polynomials than for Hermite and Legendre polynomials for the data collected on both days. This suggests that Zernike polynomials describe pupil amplitude variation more efficiently than the two other bases do because fewer terms can be used.

6 Conclusions

We have developed a framework for extraction of both the amplitude and phase components of the pupil function of an EUVL system. This method uses the images formed by that system to extract its aberrated pupil function. We have successfully demonstrated this technique to extract both components of the pupil function for a zone plate on an EUV mask microscope on two separate occasions. We found an amplitude RMS of 11% and phase RMS of 23.4 $m\lambda$ on day 1 and an amplitude RMS of 12% and phase RMS of 8.4 $m\lambda$ on day 2. It should be noted that the difference in amplitude variation is within the margin of error for this technique while the phase is not. The variation in phase RMS between day 1 and day 2 is likely due to the realignment and recalibration of the lens between the two days. This is demonstrative of the criticality of *in situ* aberration monitoring. Although the pupil amplitude variation did not change between the two days, it is necessary to adequately describe the pupil of this EUV imaging system.

The pupil amplitude function was expanded in three different orthogonal bases: (1) Zernike polynomials, (2) Legendre polynomials, and (3) Hermite polynomials. It was found that the Zernike polynomials appear to describe the pupil amplitude variation the best of these three bases. This is based on the rate at which the RMSE decreases when the pupil amplitude variation is decomposed on this basis. Hermite polynomials offer a similar RMSE decrease rate but are not rotationally invariant like the Zernike polynomials. The pupil phase variation was only expanded in Zernike polynomials in which high-order terms were lumped into a single approximate low-order term. It was shown that this results in minimal error using this technique. Discriminating between the low- and high-order terms would require a different set of metrology targets to highlight the differences between these terms.[12] Future work will study the effects of pupil amplitude variation described by Zernike polynomials on image quality, potentially identify a better basis than Zernike polynomials, and measure both amplitude and phase pupil variation from resist images.

Acknowledgments

The authors would like to thank the Semiconductor Research Corporation (SRC)/Global Research Collaboration (GRC) through Research Task 2126.001 as well as KLA Tencor for use of the PROLITH™ lithography simulator.

References

1. M. Kempsell Sears et al., "Extending SMO into the lens pupil domain," *Proc. SPIE* **7973**, 79731B (2011).
2. M. Kempsell Sears, J. Bekaert, and B. W. Smith, "Pupil wavefront manipulation for optical nanolithography," *Proc. SPIE* **8326**, 832611 (2012).
3. B. Baylav et al., "Impact of pupil plane filtering on mask roughness transfer," *J. Vac. Sci. Technol. B* **31**(6), 06F801 (2013).
4. V. Bakshi, Ed., *EUV Lithography*, SPIE, Bellingham, Washington (2008).
5. C. G. Krautschik et al., "Quantifying EUV imaging tolerances for the 70-, 50-, 35-nm modes through rigorous aerial image simulations," *Proc. SPIE* **4343**, 524 (2001).
6. L. Foucault, "Description des procédés employes pour reconnaitre la configuration des surfaces optiques," *C. R. Acad. Sci.* **47**, 958 (1858).
7. W. P. Linnik, "A simple interferometer for the investigation of optical systems," *Proc. Acad. Sci. USSR* **1**, 208 (1933).
8. P. P. Naulleau, K. A. Goldberg, and J. Bokor, "Extreme ultraviolet carrier-frequency shearing interferometry of a lithographic four-mirror optical system," *J. Vac. Sci. Technol. B* **18**, 2939–2943 (2000).
9. L. V. Zavyalova et al., "In-situ aberration monitoring using phase wheel targets," *Proc. SPIE* **5377**, 172 (2004).
10. G. L. Fenger et al., "EUVL resist-based aberration metrology," *Proc. SPIE* **8679**, 86790P (2013).
11. G. L. Fenger et al., "Extreme ultraviolet lithography resist-based aberration metrology," *J. Micro/Nanolith. MEMS MOEMS* **12**(4), 043001 (2013).
12. Z. Levinson et al., "Optimization of image based aberration metrology for EUV lithography," *Proc. SPIE* **9048**, 90482M (2014).
13. F. von Zernike, "Beugungstheorie des schneidenver-fahrens und seiner verbesserten form, der phasenkontrastmethode," *Publica* **1**, 689–704 (1934).
14. B. Nijboer, "The diffraction theory of aberrations," PhD Thesis (1942).
15. B. W. Smith, "Method for aberration detection and measurement," US Patent US7,136,143 B2 (2006).
16. E. J. Ientilucci and J. R. Schott, *Radiometry and Radiation Propagation*, 1st ed., Oxford University Press, New York, New York (2016) (in preparation).
17. V. Domnenko, T. Schmoeller, and T. Klimpel, "Analysis of EUVL mask effects under partially coherent illumination," *Proc. SPIE* **7271**, 727141 (2009).
18. C. S. Chung and H. H. Hopkins, "Influence of nonuniform amplitude on the optical transfer function," *Appl. Opt.* **28**, 1244–1250 (1989).
19. J. P. Mills and B. J. Thompson, "Effect of aberrations and apodization on the performance of coherent optical systems. II. Imaging," *J. Opt. Soc. Am. A* **3**, 704–716 (1986).
20. K. A. Goldberg et al., "Commissioning an EUV mask microscope for lithography generations reaching 8 nm," *Proc. SPIE* **8679**, 867919 (2013).
21. K. A. Goldberg et al., "Actinic mask imaging: recent results and future directions from the SHARP EUV microscope," *Proc. SPIE* **9048**, 90480Y (2014).
22. J. Gaskill, *Linear Systems, Fourier Transforms, and Optics*, John Wiley & Sons, New York, New York (1978).
23. B. W. Smith, "Optics for photolithography," in *Microlithography: Science and Technology*, 2nd ed., B. W. Smith and K. Suzuki, Eds., CRC Press, Boca Raton, Florida (2007).
24. M. Born and E. Wolf, *Principles of Optics*, 7th ed., University of Cambridge Press, Cambridge, United Kingdom (1999).
25. P. Dirksen et al., "Aberration retrieval using the extended Nijboer-Zernike approach," *J. Micro/Nanolith. MEMS MOEMS* **2**(1), 61–68 (2003).
26. S. van Haver et al., "The extended Nijboer-Zernike diffraction theory and its applications," PhD thesis (2010).
27. A. Khotanzad and Y. H. Hong, "Invariant image recognition by Zernike moments," *IEEE Trans. Pattern Anal. Mach. Intell.* **12**(5), 489–497 (1990).

28. S. Lipschutz, M. Spiegel, and J. Liu, *Schaum's Outline of Mathematical Handbook of Formulas and Tables*, 4th ed., McGraw-Hill Education, New York, New York (2012).
29. V. N. Mahajan, *Optical Imaging and Aberrations, Part III: Wavefront Analysis*, SPIE Press, Bellingham, Washington (2013).
30. KLA Tencor, "PROLITH v. X5.1," http://www.kla-tencor.com/Virtual-Lithography/dsmprolith.html (17 June 2016).
31. H. H. Hopkins, "The concept of partial coherence in optics," *Proc. R. Soc. A Math. Phys. Eng. Sci.* **208**, 263–277 (1951).
32. G. O. Reynolds et al., *The New Physical Optics Notebook: Tutorials in Fourier Optics*, American Inst. of Physics, Bellingham, Washington (1989).
33. S. L. Barnes, "A technique for maximizing details in numerical weather map analysis," *J. Appl. Meteorol.* **3**, 396–409 (1964).
34. S. Barnes, *Mesoscale Objective Map Analysis Using Weighted Time-Series Observations*, NOAA Technical Memorandum ERL NSSL-62, National Severe Storms Laboratory, Norman, Oklahoma (1973).
35. L. Zavyalova, "Measuring aberrations in lithographic projection systems with phase wheel targets," PhD Thesis (2010).

Zachary Levinson received his BS and ME degrees in microelectronic engineering from Rochester Institute of Technology (RIT), in 2013 and 2014, respectively. Currently, he is a third-year student in the Microsystems Engineering PhD program, working under the supervision of Dr. Bruce W. Smith in the RIT Nanolithography Research Laboratory. He is a member of the Optical Society of America (OSA) and SPIE.

Erik Verduijn received his licence de physique in fundamental physics from the Universit de Rouen and his MSc degree in applied physics from Eindhoven University of Technology. He is a senior member of technical staff at the Strategic Lithography Technology Department, GLOBALFOUNDRIES, and assigned to the IMEC research consortium. At IMEC, he supports GLOBALFOUNDRIES EUVL research activities related to mask defectivity, resist optimization, device integration, and printability enhancements. He has prior experience in the fields of lithography and spin electronics.

Obert R. Wood received his BS, MS, and PhD degrees in electrical engineering from the University of California at Berkeley in 1964, 1965, and 1969, respectively. He is a principal member of the technical staff at the Strategic Lithography Technology Department, GLOBALFOUNDRIES. He was a member of technical staff at Bell Laboratories for 34 years. He is author or coauthor of 271 papers, inventor or coinventor of 27 patents, and a fellow of OSA and SPIE.

Pawitter Mangat received his PhD in materials science in 1991 and his MBA degree in technology management in 2000. He is the deputy director of EUVL at GLOBALFOUNDRIES and responsible for establishing EUVL infrastructure while providing manufacturable solutions. Previously, he held leadership roles at Motorola Inc. and was a member of the SRC Board of Directors and Semiconductor Industry Association (SIA) Technology Strategy Committee. He has 27 issued patents and has coauthored 100+ publications.

Kenneth A. Goldberg received his AB degree in physics and applied mathematics, and his PhD in physics from the University of California, Berkeley. He is the deputy director of the Center for X-Ray Optics, Lawrence Berkeley National Laboratory, specializing in the development of EUV and soft x-ray technologies, including lithography, mask imaging, and wavefront measuring interferometry. He is the principal investigator of the SHARP EUV photomask imaging microscope.

Markus P. Benk received his BS degree in photo engineering from Cologne University of Applied Sciences in 2006, and his PhD from Rheinisch-Westfälische Technische Hochschule Aachen University, in 2011. He is the project scientist at the SHARP microscope, Center of X-Ray Optics, Lawrence Berkeley National Laboratory. He has authored and coauthored several papers on extreme ultraviolet and soft x-ray imaging. His current research interests include sources, metrology and optics for soft x-rays, and extreme ultraviolet light.

Antoine Wojdyla received his PhD from the École Polytechnique in 2011, where he studied time-domain phase imaging in the far infrared range. He is a postdoctoral fellow at Lawrence Berkeley National Laboratory's Center for X-Ray Optics. His research interests include optical instrumentation and computational analysis of image data.

Bruce W. Smith is a professor and the director of microsystems engineering at the RIT. He has published over 150 papers, several textbooks and chapters, and holds 27 patents in the fields of semiconductor lithography, optical systems, and microelectronics. He is a fellow of SPIE and OSA, a senior member of IEEE, a member of American Vacuum Society, and American Society for Engineering Education, and a recipient of numerous awards for teaching, research, and mentoring.